Environmental Science and Pollution Research (2022) 29:85465–85481
https://doi.org/10.1007/s11356-022-21757-y

RESEARCH ARTICLE

Modeling and assessment of CO_2 geological storage in the Eastern Deccan Basalt of India

Danqing Liu[1,2] · Ramesh Agarwal[3] · Fang Liu[1] · Sen Yang[1] · Yilian Li[1]

Received: 2 March 2022 / Accepted: 26 June 2022 / Published online: 7 July 2022

Abstract

In this study, the CO_2 carbonatization potential of the Deccan basalt formation in Eastern India is evaluated by establishing a hydro-chemical field-scale model based on the geological, hydrological, and geochemical parameter of the basalt in the Mandla lobe. The reliable initial mineral thermodynamic parameters are obtained by validating the laboratory scale experiment of CO_2-water-basalt reaction with a numerical method. Over 50% of injected carbon mineralized within 140 days for the Deccan basalt in the Mandla lobe, and the majority of CO_2 is sequestered as ankerite, siderite, and calcite, which occupy a percent of 65%, 28%, and 7%, respectively. Clay minerals, including smectite and chlorite, are important secondary minerals contributing to the process of CO_2 storage in the basaltic reservoir. Clay precipitation can promote the dissolution of silica- and aluminum-rich plagioclase and release Ca^{2+} to enhance the carbonatization of CO_2 to Ca carbonates but competes for Fe^{2+} and Mg^{2+} from siderite and magnesite. Clay precipitation also impacts the CO_2 carbonatization efficiency by changing the basalt conductivity. CO_2 carbonatization efficiency was found to increase with the reduction of injection rate. However, slow flow rate can increase the pore clogging risk and induce large pressure build-up. This is the first field-scale assessment of CO_2 mineralization potential of the Deccan basalt, which is one of the largest terrestrial flood basalt formations in the world. The results can provide valuable information and scientific support for India and global carbon mitigation.

Keywords Aqueous CO_2 · Deccan basalt · Assessment of GCS · Clays · Injection rate

Introduction

The Energy & Climate International Unit has published a report that the carbon emissions must be reduced in order to halt climate change. Currently, the reduction in carbon emissions is not sufficient and the "net zero emission" has been proposed (Unit 2020). To realize the global carbon neutrality as soon as possible, every country of the world should respond rapidly and design an appropriate strategy to take the needed action. CO_2 emission reduction by geological sequestration is regarded as an important and efficient strategy. In the scenario of CO_2 storage under the subsurface, CO_2 can be sequestered by physical mechanisms such as structural trapping, residual trapping, and adsorption trapping, and can also be immobilized with dissolution and mineralization. CO_2 carbonatization is a key process of the global carbon cycle in which atmospheric CO_2 is stored (Berner and Raiswell 1983), which is also recognized as the safest way to store CO_2 in the subsurface since the resulting carbonate minerals are stable and provide environmentally low risk over geological time scales (Ragnheidardottir et al. 2011).

Basaltic rock is one of the most promising reservoirs for efficient and rapid CO_2 carbonatization, when compared with the conventional CO_2 storage sites, e.g., the deep saline aquifers, depleted oil/gas reservoirs, unconventional shale gas reservoirs, and coal-bed methane reservoirs (Zhu et al. 2016). Basalt is a type of rock containing abundance of minerals such as olivine and pyroxene which are rich in Ca, Mg, and Fe bearings, which is the source

Responsible Editor: V.V.S.S. Sarma

✉ Danqing Liu
liudq@cug.edu.cn

[1] School of Environmental Studies, China University of Geosciences, Wuhan 430074, China

[2] State Key Laboratory of Biogeology and Environmental Geology, China University of Geosciences, Wuhan 430074, China

[3] Washington University in St. Louis, 1 Brookings Dr., St. Louis, MO 63130, USA

of precipitation of carbonates including calcite, aragonite, magnesite, siderite, ankerite, and dolomite (Li et al. 2004; Nicolas et al. 2003). Studies of basalt-CO_2 interactions in aqueous media indicated that pyroxene dissolution in the acidic aqueous can release Mg^{2+} ions to form magnesite (Gislason 2001), while plagioclase can release Ca^{2+} to form calcite through dissolution (Nicolas et al. 2003). It is estimated that ~ 60% of the global surface is occupied by basalt and the total CO_2 storage capacity in basalt from the deep-sea can be as high as ~ 13800 to 127800 Gt (Gislason et al. 2010; Marieni et al. 2013). Basalt-CO_2 reaction can occur rapidly. The onshore pilot project of CO_2 sequestration in basalt conducted at the Hellisheidi geothermal power plant in Iceland, the so-called CarbFix project, initiated the injection of CO_2 in January 2012. Two hundred thirty tons of CO_2 was co-injected with 7000t of H_2O into the targeted basalt formation which is composed of basalt lavas with an olivine tholeiitic composition with an age ranging from 500,000 to 125,000 years before present (Callow et al. 2018). It was observed that > 95% of the injected CO_2 mineralized within a couple of months of the initial CO_2 injection (Matter et al. 2016). Apart from basalt from the Carbfix project, it has been reported that CO_2–H_2O mixtures were allowed to react with the Columbia River, Central Atlantic Mafic, Newark Basin, Karoo, and Deccan basalt (Kumar and Shrivastava 2019a).

The Deccan basalt from India is one of the largest terrestrial flood basalt formations in the world which has immense accumulations of tholeiitic basalt magmas erupted over a relatively short time span straddling the Cretaceous-Tertiary boundary (Pattanayak 2002; Shrivastava et al. 2014). The isolated Mandla lobe, located in northeast of the Deccan volcanic province, is reported to have 37 major petrography distinct lava flows spread in the ~ 900-m-thick volcano-sedimentary sequences, and the uppermost part of the lava flow is highly vesicular which can provide structural pathways for CO_2 and are conducive to CO_2 sequestration. The availability of CO_2 emission sources around the Deccan basalt is also a requisite for the feasibility of CO_2 storage (Abraham-A and Tassinari 2021). It is reported that 26% of the total coal-fueled generation capacity in India is located on or in close proximity to the Deccan basalts (McGrail et al. 2006). According to the IPCC report (2005), power generation by coal combustion is the largest source for generation of CO_2 (78% of the CO_2 produced by large sources) (Talman 2015).

In recent years, several experimental and numerical studies on the CO_2 storage in the Deccan basalt have been conducted. Shrivastava's research group conducted lab-scale experiment of Deccan flood basalt specimens from the Eastern Mandla lobe reacting them with CO_2 under different pressure (5 and 10 bars) and temperature in a time duration of 50, 60, 70, and 80 h (Kumar and Shrivastava 2019a; Rani et al 2013). They also studied the long-term CO_2 capture-induced calcite crystallographic changes in Deccan basalt (Kumar and Shrivastava, 2019a). Prasad et al. (2009) reported the laboratory-scale experimental results to determine the CO_2 sequestration potential of picritic basalts from the Deccan basalt volcanic province Maharashtra. Shrivastava and Pathak (2016) and Kumar and Shrivastava (2019b) have obtained both experimental and numerical results of CO_2-water-Deccan basalt reaction from the Mandla lobe. Kumar et al. (2017) employed the transition-state-theory based on numerical model to simulate the basalt-CO_2-water-saturated interaction under hydrothermal-like conditions in the Deccan basalt. However, the purpose of these computational simulations was to explain the experimental results from the point of view of mineral thermodynamic reactions.

The acid dissolution of silica-aluminum minerals such as plagioclase and pyroxene not only releases divalent cations to promote carbonate precipitation, but also releases abundance of silica and aluminum at the same time. The combination of irons enriched from the dissolution of basalt under mildly acdic conditions tends to lead to the formation of clays and zeolites. Clays, zeolites, and oxides are widely observed to co-precipitate with carbonates in the context of CO_2-water-basalt reactions, and reported to clog narrow fractures and pore throats of the basalt potentially reducing permeability and reservoir conductivity thus to change the transport of fluid in the subsurface. Mineral precipitation in natural joints and fractures in basalt has been observed to partly or fully inhibit fluid flow. The transport of CO_2 can dictate both the speed and extent of mineral carbonatization which would impact the CO_2 storage potential (Andreani et al 2009; Liu et al. 2019; Menefee et al. 2017; Peuble et al 2015). As a result, to comprehensively and accurately assess the CO_2 storage potential of the Deccan basalt, it is critical to combine CO_2-water-basalt reaction with fluid transport and consider the effect of clay precipitation.

The specific objective of this study is to evaluate the CO_2 mineralization potential of the Deccan basalt from the Eastern India. The laboratory-scale experiment of CO_2-water-Deccan basalt reaction at different CO_2 pressures conducted by Kumar and Shrivastava (2019c) is first reconstructed with the numerical method to obtain the appropriate mineral thermodynamic parameters. Based on the validated lab-scale model, a 2-D homogeneous field-scale model with size of 200 m in horizontal and 120 m in vertical direction is then established by collecting needed hydrological data of the Deccan basalt from the Mandla lobe. A total of 1.2096×10^4 tons of CO_2 dissolved water (equivalent to 184.24 tons of carbon) is injected into the Deccan basalt at a rate of 1.0 kg/s for 140 days. By controlling the existence of clay minerals especially smectite and chlorite, role of clay minerals on CO_2 carbonatization efficiency and fluid transport in the Deccan basalt are explored. In addition, impact of fluid flow rate on CO_2 carbonatization and

reservoir pressure perturbation is also discussed. It should be noted that although this study is based on a specific site, uncertainty exists in the selection of the represented basalt mineral composition, reservoir porosity, permeability, initial pressure and temperature, etc.; the obtained conclusions still provide important guidance for the CO_2 geological sequestration potential in India.

Material and methods

Geological background of the Mandla lobe basalt

The Deccan volcanic province is an important large igneous province in the world. It marks the Cretaceous-Palaeogene boundary which witnessed the global climate and bio-geosphere change (Keller et al. 2008). The Deccan volcanic province constitutes one of the largest continental flood basalt in the world which covers a large part of the peninsular India with an area of nearly 500,000 km^2 (Krishnamurthy 2020). As an isolated lobe, the Mandla lobe is located in northeast of the Deccan volcanic province and extends over a distance of 344 km in the E-W strike direction and 156 km across the N-S direction (Fig. 1). It is tectonically controlled by the rift-bounded basin fault system of the Son-Narmada and Tapi rivers in the north and south of the Manda lobe, respectively. Furthermore, it lies towards the southeastern part of the central Indian Suture Zone.

On the basis of regional mapping, physical characters, petrography, and lateral tracing of the lava flows, there are 37 major petrography distinct lava flows spread in the ~ 900-m-thick volcano-sedimentary sequences around Mandla. Among all different lava flows, the fourth lava flow of the eastern Deccan basalt is found to have plentiful columnar and jointed structures. They are often marked with prolific cracks and possess well-developed colonnade and entablature structures within the lava flow. It is reported that the uppermost part of the lava flow is highly vesicular which can provide structural pathways for CO_2 and are conducive to CO_2 sequestration.

Simulator description

TOUGHREACT is employed to conduct the reactive transport modeling. The details of the code's capabilities, governing equations, calculation procedures, and limitations are available in the user's manual. All flow and transport equations are obtained based on the principles of mass and energy conservation. The detailed discussion on models for fluid and heat flow can be found in Pruess (1991) and Pruess et al. (1999).

Geochemical reaction calculation

For geochemical calculation, a subset of aqueous species is selected as basis species, and all other species including aqueous complexes, minerals, and gaseous species are called secondary species (Steefel 1994; Yeh and Tripathi 1991). Chemical transport equations are derived from the total dissolved concentration of chemical components which is the sum of their basis species and their associated aqueous secondary species. The advection and diffusion mechanisms are considered for the chemical transport calculation. The kinetic rate law is employed to describe the mineral dissolution and precipitation reactions, the expression of which (Eq. (1)) is referenced to Lasaga et al. (1994). At each time step, the reaction rate constants, k_n; total surface area,A_n; and the kinetic mineral saturation ratio, Ω_n of each mineral are used to calculate the overall reaction rate. The positive values of r_n in Eq. (1) indicate dissolution and negative values stand for precipitation. The explanation of each parameter is included in the nomenclature.

$$r_n = \mathrm{f}\left(\mathrm{c1}, \mathrm{c2}, \ldots, c_{N_c}\right) = \pm k_n A_n \left|1 - \Omega_n^{\theta}\right|^{\eta} \tag{1}$$

The reaction rate constants considered here are calculated based on the reaction rate constant at 25℃, k_{25}, and activation energy, E_{a}, with different mechanisms through model calibration or published by other authors (Eq. (2)). The mechanisms include the neutral, acid, and base mechanisms. For the acid and base mechanisms, dissolution and precipitation of minerals are catalyzed by H^+ and OH^- respectively.

$$k_n = k_{25}^{\mathrm{nu}} \exp\left[\frac{-E_a^{\mathrm{nu}}}{R}\left(\frac{1}{T} - \frac{1}{298.15}\right)\right] + k_{25}^{\mathrm{H}} \exp\left[\frac{-E_a^{\mathrm{H}}}{R}\left(\frac{1}{T} - \frac{1}{298.15}\right)\right] a_{\mathrm{H}}^{\sigma_{\mathrm{H}}} + k_{25}^{\mathrm{OH}} \exp\left[\frac{-E_a^{\mathrm{OH}}}{R}\left(\frac{1}{T} - \frac{1}{298.15}\right)\right] a_{\mathrm{OH}}^{\sigma_{\mathrm{OH}}} \tag{2}$$

Mineral reaction–induced porosity and permeability changes

The porosity changes due to mineral alterations are described with the following expressions in the simulator (Xu et al. 2006):

$$\varnothing_i = 1.0 - \sum_{m=1}^{k} F_k^i - F_n^i \tag{3}$$

A simplified Kozeny-Carman equation was implemented to describe the relation between porosity and permeability.

$$\frac{k_i}{k_0} = \left(\frac{\varnothing_i}{\varnothing_0}\right)^3 \times \left(\frac{1 - \varnothing_0}{1 - \varnothing_i}\right)^2 \tag{4}$$

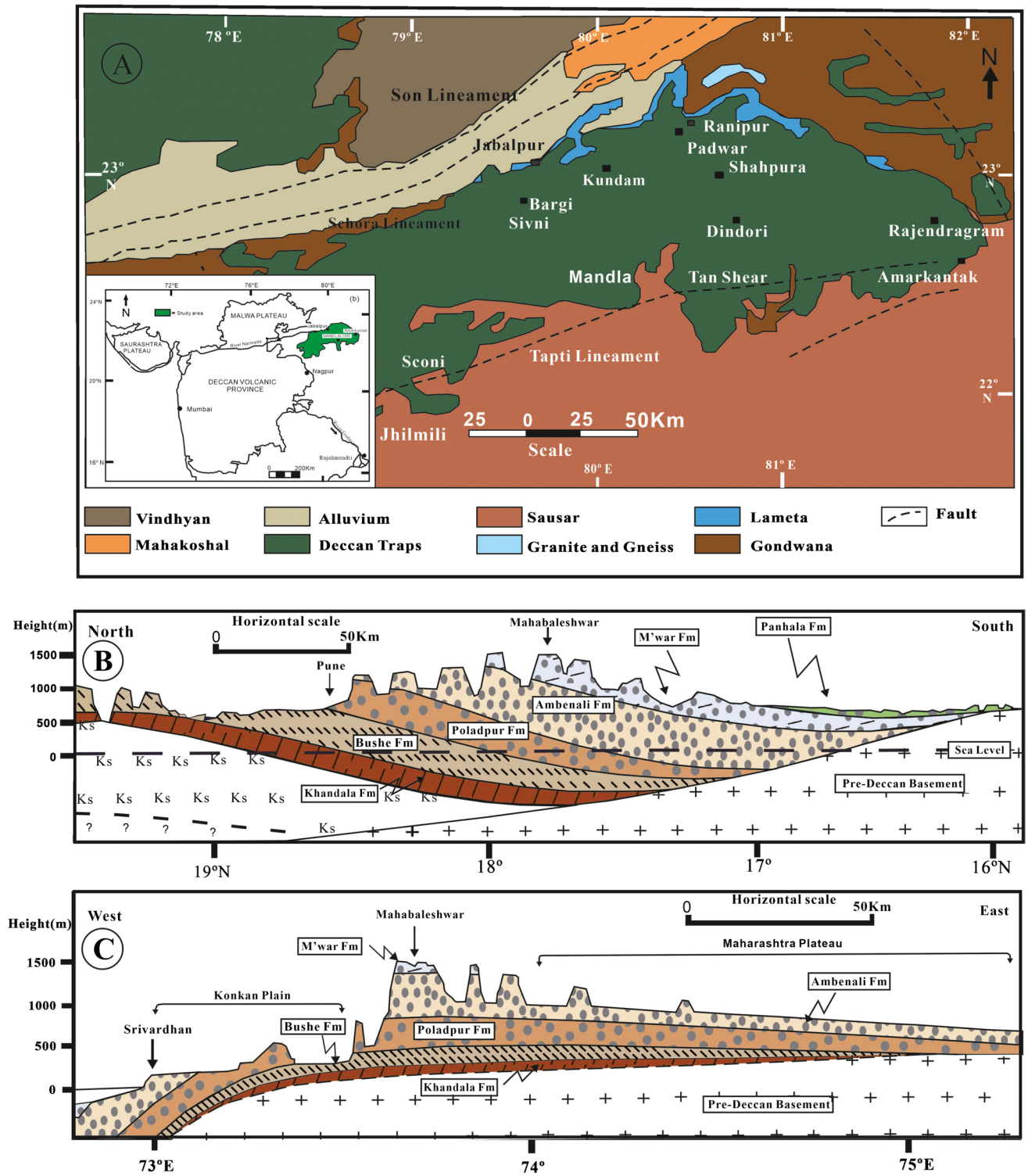

Fig. 1 Location of the Mandla lobe in the eastern Deccan volcanic province and Geological section of the Deccan basalt from north to south (**A**) and west to east (**B**) (Revised according to Krishnamurthy 2020)

Initial mineral and water chemistry

For regional-scale reactive-transport modeling, the credibility of results is dependent on the initial mineral composition and its thermodynamic data. To obtain the representative mineral composition of the Deccan basalt from the Mandla lobe, the CO_2 sequestration experiment conducted by Kumar and Shrivastava (2019c) was reconstructed with numerical method. To perform the high pressure–temperature experiments, 10-g hypocrystalline and vesicular basalt specimen from the Mandla lobe and 100 ml of deionized water were kept inside a 600-ml columned reactor with a height of 0.12 m and diameter of 0.08 m. The reaction temperature was set as 100 and two scenarios of pCO_2 at 5 bar and 10 bar were explored respectively as shown in Fig. 2(A).

To mimic the experimental condition, the section of column reactor filled with water was considered equivalent to 41 grids in vertical direction as shown in Fig. 2(B), with size of 0.07 m × 0.07 m × 0.0005 m. It was assumed that 10 g of basalt specimens in the experiment was completely homogeneously distributed in the deionized water, and the porosity can be calculated as 96%. A pressure boundary consisting of pure water equilibrated with CO_2 at a constant pressure of 5 bars and 10 bars and temperature of 100℃ was imposed at the top inlet to match experimental condition. A no-flux boundary was set at the bottom and lateral direction of the model to represent the sealed wall of the reaction vessel.

As reported by Kumar and Shrivastava (2019c), the experimental basalt was composed of pyroxene, plagioclase, magnetite, olivine, chlorophaeite, and glass. But only the volume fraction of clinopyroxene as 44.75% was given. During the model calibration, we found that olivine is very critical to match the rapid decline of pH; as a result, 3% fayalite and 2% forsterite were added in the primary minerals to represent olivine and the ratio of fayalite:forsterite was determined based on the Fe:Mg = 0.38:0.29 in olivine. Because the clinopyroxene is usually composed of diopside and hedenbergite, these two minerals were selected to represent pyroxene and the content of diopside and hedenbergite was calculated according to the molar ratio of Fe:Mg = 0.24:0.19 in clinopyroxene. Albite, anorthite, and k-feldspar were set to represent plagioclase, glass, and other minerals. The ratio Ca:Na = 0.016484:0.00665 of the Ca plagioclase in the original basalt specimens was kept for anorthite and albite. The volume fraction of k-feldspar and magnetite was set as 0.0025 and 0.0955 according to the calculation of Kumar and Shrivastava (2019c).

The choice of secondary precipitated minerals is also crucial for the model validation. The observed secondary minerals in the experiments include carbonates such as aragonite, calcite, ankerite, siderite, magnesite, some phyllosilicates like chlorite and saponite, and also some wustite. To accurately depict the CO_2-water-basalt interaction at different CO_2 partial pressures, all these minerals were selected as the secondary

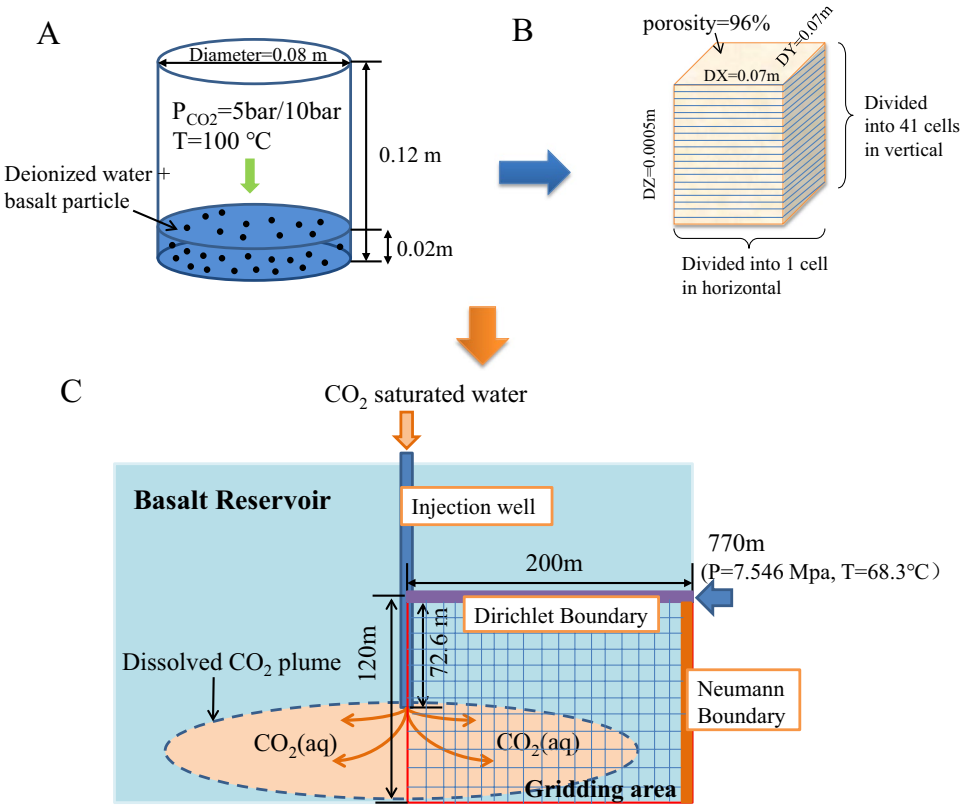

Fig. 2 Schematic of the simulation lab-scale model and field-scale model. (**A**) The generalization of the lab-scale model from the experiment and (**B**) the gridding of the mesh, and (**C**) the concept map of the field-scale model. The mineral thermodynamic data calibrated through the lab-scale simulation was implemented directly into the field-scale model

minerals. Because of the richness of Ca, Na, and Mg in this basalt, Ca-smectite, Na-smectite, and Mg-smectite were all included in the secondary minerals list.

To validate the simulation model with the experimental results, the major source of uncertainty comes from the mineral reaction kinetic parameters including kinetic constants at 25℃, activation energy, and reactive surface area. The mineral reaction kinetic parameters of the major primary and secondary minerals were obtained by adjusting the aqueous pH of the model to fit the experimental results; these are listed in Table 1. To accelerate the CO_2-rock reaction rate, the experiments is conventionally conducted at stirring condition which will enhance the gaseous and aqueous diffusion rate, but not impact the mineral reaction kinetics. As a result, the aqueous diffusion coefficient was enhanced into two orders of magnitude larger than the 7.5×10^{-9} m^2/s (Cadogan et al 2014).

Field-scale model establishment

It was mentioned previously that the fourth lava flow of the eastern Deccan basalt shows columnar and jointed structures and the uppermost part of which is highly vesicular which can provide structural pathways for CO_2. The forth lava flow was selected as the target CO_2 storage site. Because some of the specific properties related to CO_2 storage efficiency are not available for this formation, some approximate data were employed. The contact between the base of the basalt in the Mandla lobe and underlying sedimentary beds is at 364 m above mean sea level near Jabalpur and the maximum elevation of basalts is 1177 m at Badargarh (Shrivastava et al. 2014). In the simulation, an average elevation of 770 m and a thickness of 100 m for the basalt formation were selected. The normal pressure gradient of 9.81 MPa/km and the average geothermal gradient of the Deccan basalt in Jabalpur of the Mandla lobe (4.25℃/100 m) (Srinivas et al. 2019) were employed.

A large numbers of studies on the Deccan basalt's petrophysical and hydrological conditions have been conducted for the central part, but are missing for the eastern part. It is reported that the Mandla lobe has Ambenali- and broadly Poladpur-like formation characteristics similar to the central part. Perumal (2014) have collected fresh samples of the Deccan basalt to document the variation in physical properties of the rock with depth within and between rock formations that are arranged in the Deccan basalt stratigraphic sequence and the basement rocks. The porosity of basalt varies between 0 ~ 6.3%; as a result, a relatively large porosity of 6.3% were used in the CCS field-model establishment. Some of the other needed information for the field-model establishment was directly obtained as the average value of the other part of the Deccan basalt. The detailed parameters can be found in Table 2.

A 2-D rectangular model with lateral distance of 200 m and vertical depth of 120 m was established to simulate the CO_2 storage potential in the field-scale Deccan basalt (Fig. 3). The grid size was equally divided into 5 m × 5 m × 5 m, and the total grids were 40 in horizontal and 24 in vertical direction. The top side was set as a constant boundary by assigning infinite volume to those grids. The bottom boundary was set as no-flux boundary. The CO_2 saturated water was injected from the left side at a depth of 72.6 m, while groundwater flowed out from the right side at a typical groundwater flow rate of 10^{-5} kg/s/m^2 (USGS, 2020).

Initial water and boundary water

Except for the initial hydrological data, the initial chemical condition of the formation water is also a requisite for the reactive transport modeling. Because of lack of directly drilled groundwater data for the Mandla lobe basalt, 72 groundwater sample compositions collected under phreatic conditions in the weathered zone, fractured and vesicular basalts, and under semi-confined to confined conditions in the fractured zone from the northern part of the Deccan plateau were utilized (Pawar et al. 2008). The average pH of pre-monsoon and post-monsoon season of 7.86 was employed for the groundwater of Mandla lobe basalt in this simulation. To accelerate CO_2 and basalt reaction rate, the water and CO_2 are mixed at a designated point in the borehole ($P = 7.546$ MPa, $T = 57$℃). The injecting water composition was calculated with PHREEQC; the detailed determination method can be found in SI. The water saturated with CO_2 at a pressure of nearly 7.7 MPa at the bottom of the established model will then be injected at a rate of 1 kg/s for 140 days. The detailed information of the initial water and boundary water is listed in Table 2.

Simulation scenarios setup

A total of 1.2096×10^4 tons CO_2 dissolved formation water (equivalent to 184.24 tons of carbon) was injected into the Deccan basalt reservoir at an injection rate of 1 kg/s in the duration of 140 days (scenario 1 and named as case_base). To assess the CO_2 carbonatization potential of the Deccan basalt in the Mandla lobe and elucidate the impact of other alumino-silicate minerals' precipitation and injection rate on CO_2 storage efficiency, another two scenarios were set up. In scenario 2, four simulation cases were set up to explore the impact of clay precipitation on CO_2 mineralization and migration by controlling the existence of clays as the secondary minerals. In scenario 3, another four simulation cases with different injection rate of 0.4 kg/s, 0.5 kg/s, 2.0 kg/s, and 3.0 kg/s were added based on the baseline cases to analyze the sensitivity of

Table 1 Summary of primary and secondary mineral specific surface area and reaction kinetics

Minerals	Volume fraction (%)	Specific surface area (cm^2/g)	Acid mechanism			Neutral mechanism		Basic mechanism		
			log k_{25} ($mol/m^2/s$)	E_a (kJ/mol)	n^{H+}	log k_{25} ($mol/m^2/s$)	E_a (kJ/mol)	log k_{25} ($mol/m^2/s$)	E_a (kJ/mol)	n^{OH+}
Primary mineral										
Diopside	19	340[b]	− 6.36[a]	96.1[a]	0.71[a]	− 11.11[a]	40.6[a]	–	–	–
Hedenbergite	25	34[c]	− 6.36[c]	22.97[c]	0.71[c]	− 11.11[c]	9.7[c]	–	–	–
Albite	12	225[d]	− 10.16[a]	65.0[a]	0.457[a]	− 12.56[a]	69.8[a]	− 15.6[a]	71.0[a]	− 0.572[a]
Anorthite	29	225[d]	− 3.5[a]	16.6[a]	1.411[a]	− 9.12[a]	17.8[a]	–	–	–
Forsterite	2	1800[b]	− 6.85[a]	16.06[a]	0.47[a]	− 10.64[a]	18.08[a]	–	–	–
Fayalite	3	2000[b]	− 4.85[a]	22.56[e]	0.47[e]	− 12.8[e]	22.56[e]	–	–	–
Magnetite	9.55	9.8	− 8.59[a]	18.6[a]	0.279[a]	− 10.78[a]	18.6[a]	–	–	–
Glass and others (K-feldspar)	0.25	190[d]	− 9.45[c]	12.41[c]	0.5[c]	− 12.41[c]	9.08[c]	− 21.2[c]	9.08[c]	− 0.823[c]
Secondary mineral										
Aragonite	0.00	370[f]	− 0.3[a]	3.44[a]	1.0[a]	− 5.81[a]	5.62[a]	− 3.48[a]	35.4[a]	1.0[a]
Calcite	0.00	370[g]	− 0.3	3.44	1.0	− 5.81	15.62	− 3.48	35.4	1.0
Magnesite	0.00	662[f]	− 6.38[a]	3.44[a]	1.0[a]	− 9.34[a]	5.62[a]			
Ankerite	0.00	98	− 3.76[h]	36.1[h]	0.5[h]	− 8.23[h]	37.2[h]	− 5.11[h]	34.8[h]	0.5[h]
Siderite	0.00	1050[c]	− 3.74[c]	13.38[c]	0.9[c]	− 8.90[c]	15.0[c]	–	–	–
Chlorite	0.00	0.98	− 12.11[i]	48[i]	0.5[i]	− 14.52[i]	48[i]			
Ca-smectite	0.00	10.87	− 10.98[a]	23.6[a]	0.34[a]	− 15.78[a]	35.0[a]	− 17.52[a]	58.9[a]	− 0.4[a]
Na-smectite[j]	0.00	10.87	− 10.98	23.6	0.34	− 15.78	35.0	− 17.52	58.9	− 0.4
Mg-smectite[j]	0.00	10.87	− 10.98	23.6	0.34	− 16.78[k]	35.0	− 17.52	58.9	− 0.4
Amorphous silica	0.00	225[c]	–	–	–	− 9.7[c]	18.88[c]	–	–	–

[a]Palandri and Kharaka (2004)

[b]Mineral specific surface area revised from Liu et al. (2019) in calibrating the lab-scale model

[c]Liu et al. (2019)

[d]Menefee et al. (2017)

[e]Xiong et al. (2017)

[f]Pokrovsky et al. (2005)

[g]The kinetic and specific surface area of calcite are assigned to aragonite

[h]The kinetics and specific surface area of dolomite (Palandri and Kharaka 2004) are assigned to ankerite

[i]The kinetics parameters are revised from Palandri and Kharaka (2004) in calibrating the lab-scale model

[j]The kinetic and specific surface area of smectite-Ca are assigned to smectite-Na and smectite-Mg

[k]The kinetic of smectite-Mg is revised to calibrate the lab-scale model

Table 2 Data used in field-scale model

Physical data			
Parameters	Value		Source
Depth/m	770 m (364 ~ 1177) m		Shrivastava et al. (2014)
Thickness/m	120 m		
Rock density	2.91		Perumal (2014)
Porosity	6.3%		Perumal (2014)
Permeability	10 mD		Manning and Bird (1995)
Pressure gradient	9.81 MPa/km		
Pressure	7.546 MPa/74.5 atm		
Geothermal gradient	4.25 ℃/100 m		Srinivas et al. (2019)
Temperature	57℃		
Water chemistry data			
Index	Initial water (mole/kg H_2O) (Pawar et al 2008)		Boundary water (mole/kg H_2O)
pH	7.585		3.422
Ca	4.3000×10^{-4}		
Mg	3.4396×10^{-4}		
Na	6.0565×10^{-4}		
K	7.3077×10^{-6}		
Fe	5.3571×10^{-6}		
SiO_2	4.1000×10^{-4}		
HCO_3	1.4393×10^{-3}	6.4250×10^{-1}	
Al	7.4074×10^{-6}		
SO_4	8.0365×10^{-5}		
Cl	4.8028×10^{-4}		

injection rate on CO_2 carbonatization efficiency and security. The total injected CO_2 capacity was kept the same for all the cases. The specific simulation case setups are summarized in Table 3.

CO_2 mineralization efficiency calculation

During the field-scale simulation, the individual carbonates' volume fraction of each grid can be generated automatically; as a result, the total mass of carbon m_k^t in precipitated carbonates k at time t can be calculated by Eq. (5), and the total dissolved inorganic carbon (DIC) at time t can be calculated by Eq. (6). Then the CO_2 mineralization efficiency (E) can be obtained accordingly as shown in Eq. (7).

$$m_k^t = \sum_i^n aV_i F_k^i \rho_k / M_k \tag{5}$$

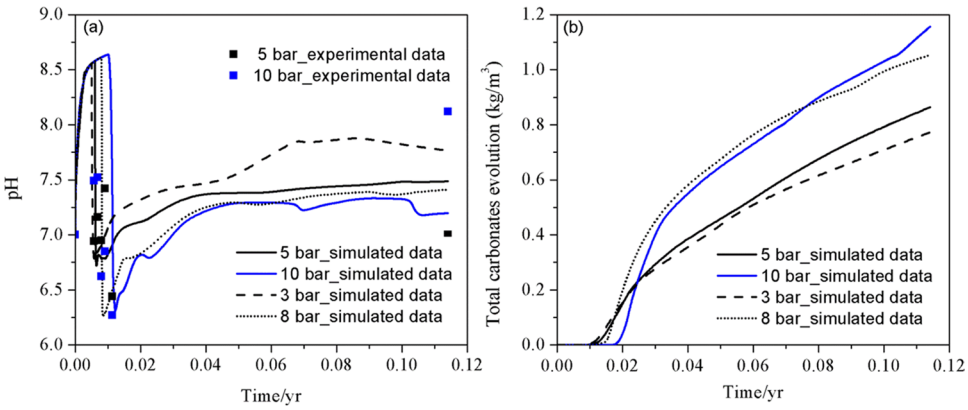

Fig. 3 Comparison of pH evolution (**a**) and total CO2 sequestered in mineral phase (**b**) at CO2 pressure of 3.0 bars, 5.0 bars, 8 bars, and 10 bars. The experimental data on pH evolution at CO2 pressure of 5 bars and 10 bars is also plotted in sub-figure (a)

Table 3 Simulation model setup

Name		Existence of clay minerals	Clay type	Response of porosity on fluid	Injection rate/ (kg/s	Purpose
Scenario1	Case_base	√	Smectite + chlorite	√	1.0	Baseline
Scenario2	Case_sm	√	Smectite	√	1.0	Competition of clays
	Case_chl	√	Chlorite	√		
	Case_wcnp	√	Smectite + chlorite	/		
	Case_ncwp	/	/	/		
Scenario3	Case_r1	√	Smectite + chlorite	√	0.4	Impact of injection rate
	Case_r2	√	Smectite + chlorite	√	0.5	
	Case_r3	√	Smectite + chlorite	√	2.0	
	Case_r4	√	Smectite + chlorite	√	3.0	

$$m_{\mathrm{DIC}}{}^{t} = rt\left(c^{\mathrm{inj}}_{\mathrm{co2(aq)}} + c^{\mathrm{inj}}_{\mathrm{hco3-}}\right) + \sum_{i}^{n} 12 p_i^0 V_i \rho_{iw}^0 \left(c^{\mathrm{ini}}_{\mathrm{co2(aq)}} + c^{\mathrm{ini}}_{\mathrm{hco3-}}\right) \quad (6)$$

$$E = \frac{\sum_k^l m_k^t}{m_{\mathrm{DIC}}{}^{t}} \quad (7)$$

Results

Benchmark-model calibration and lab-scale CO_2 carbonization

To obtain the appropriate mineral reaction kinetics of the field-scale model, the high temperature and pressure CO_2-water–rock reaction experiment based on the Deccan basalt samples collected from the Mandla lobe was calibrated with modeling. The pH variation with time at CO_2 pressure of 5 bars and 10 bars in the modeled system was compared with the experimental results as shown in Fig. 3. To further analyze the variation in carbonization efficiency with CO_2 pressure, two additional lab-scale simulation cases with CO_2 pressure of 3 bars and 8 bars were also conducted. The pH evolution in both the experiment and simulation is in good agreement at short time, e.g., within 100 h. But for a longer time of 1000 h, the simulation results only capture the pH variation tendency and possess a deviation of 6.9% and 11.4% for 5 bars and 10 bars separately.

pH is an important index to illustrate the geochemical reaction between CO_2 and basalt. As shown in Fig. 3, within the reaction period of 1000 h, pH of the system fluctuates with time. Pyroxene and olivine respond rapidly to CO_2 injection; they dissolve and release significant Ca^{2+}, Mg^{2+}, and Fe^{2+} and consume H^+. Because of this interaction, pH increases continually in the first 3 days. CO_2 dissolving into water can not only provide H^+ needed by the pyroxene and olivine, but also provide enough HCO_3^-, which to some extent can precipitate with the divalent ions, Ca^{2+}, Mg^{2+}, and Fe^{2+}, to form calcite, aragonite, siderite, and ankerite, for example. In addition, the precipitation of carbonates can release H^+ into the system at the same time, and the decrease in pH observed in Fig. 3 was mainly caused by the precipitation of these carbonates. Higher CO_2 pressure induces more acidified system in the beginning which can lead to more pyroxene and olivine dissolution. It provides more divalent cations and promotes the mineral carbonatization of CO_2. However, there is an exception for the case of CO_2 pressure at 8 bars. The minimum pH at this condition is about 6.26, which was even lower than the case with CO_2 pressure at 10 bars. The reason lies in that more carbonates precipitated at 8 bars; they lead to more H^+ releasing into the system as shown in Fig. 3b.

The major precipitated carbonates of the Deccan basalt when reacted with CO_2 at low CO_2 pressure are aragonite, calcite, ankerite, siderite, and small amount of magnesite (Fig. S1 in SI). Kumar and Shrivastava (2019c) reported that at 100℃, the XRD analysis shows the formation of calcite > ankerite > aragonite > siderite when CO_2 pressure was 5 bars and 10 bars, which is in agreement with the simulation results. In addition to carbonates, some clay minerals, zeolite, and oxides were also observed both in the experiment and in the simulation. Within the experiment, the formation of chlorite, saponite, chabazaite, and wustite was observed. The precipitation of these minerals will compete with carbonates for Ca^{2+}, Mg^{2+}, and Fe^{2+}, and their presence has been widely reported from experiments, modeling, and field observations (Gysi and Stefánsson 2012a; b; Snæbjörnsdóttir et al 2018; Wolff-Boenisch and Galeczka 2018). All studies agree that the precipitation of clays, oxides, or zeolites will clog narrow fractures and pore throats of the basalt, potentially reducing permeability and CO_2 injectivity. Such physical alterations are critical in predicting ultimate CO_2 trapping potential of

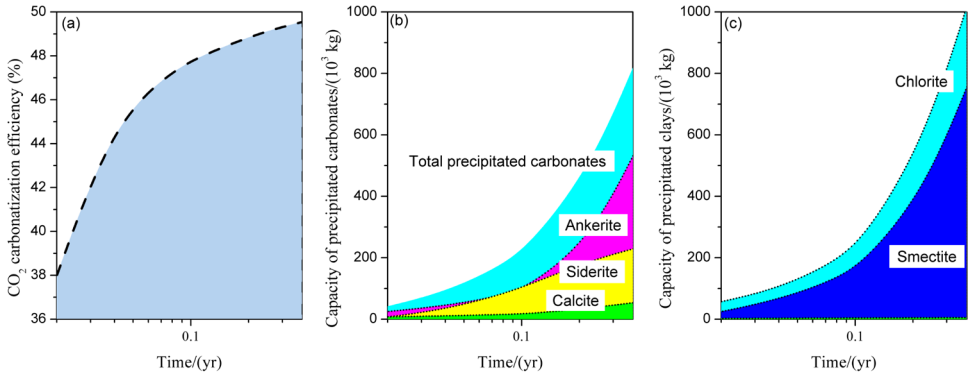

Fig. 4 Evolution of CO2 mineralization efficiency (**a**) and the major precipitated carbonates (**b**) and clays (**c**) for the Deccan basalt from the Mandla lobe, India

a basalt reservoir. However, this competition was only observed in limited spatial and temporal scale through experiments. To elucidate the large-scale aqueous CO_2 storage potential of the Deccan basalt, a two-dimensional field-scale model was established based on this calibrated model.

Field-scale CO_2 carbonatization

Baseline case

A total of 1.2096×10^4 ton CO_2 saturated water was injected into the 2-D field-scale Deccan basalt model at a rate of 1.0 kg/s for 140 days. The DIC concentration of the injected water, which is 1.285 mol/kg H_2O, was obtained with PHREEQC equilibrium calculation at 74.5 atm. and 57 ℃. It denotes that a total of 184.24 tons carbon has been injected at 140 days. Over 50% of injected carbon mineralized within 140 days for the Deccan basalt in the Mandla lobe was observed (as shown in Fig. 4). The total precipitated carbonates, including ankerite, siderite, and calcite, are 818.18 tons when CO_2 injection stopped. Apart from those carbonates, significant clays including chlorite and smectite also precipitated and the capacity of which was equivalent to 1784.42 tons at 140 days.

Cases with different setting on secondary mineral precipitation

To quantify the competition of clay precipitation on CO_2 carbonatization and explore the effect of chlorite and smectite, the results of base_case, case_ncwp, case_chl, and case_sm were compared (as shown in Table 4). By comparison, the precipitation of chlorite and/or smectite promoting the carbonatization of CO_2 was observed in this study. Limiting the formation of chlorite and/or smectite, the CO_2 carbonatization efficiency decreased from 49.55 to 49.24%, 48.92%, and 44.23%, respectively. Figure 5 shows the capacity evolution of the major precipitated carbonates and dissolved divalent source minerals. Chlorite precipitation promotes the dissolution of the majority divalent source minerals including diopside, fayalite, and forsterite by releasing H^+ into the system as well, which echoed well with the pH evolution of different simulation cases as shown in Fig. S2 in SI. The chlorite precipitation reduced the total predicted siderite mass by ~ 24% after 140 days. Similarly, the competition of Ca^{2+} between smectite and calcite was also observed as shown in Fig. 5(b), and ~ 49%

Table 4 Summary of the CO_2 carbonatization capacity of different simulation cases

Time/day	Case_base		Case_sm		Case_chl		Case_ncwp		Case_wcnp	
	Capacity[a]	Ratio[b]	Capacity[a]	Ratio[b]	Capacity[a]	Ratio[b]	Capacity[a]	Ratio[b]	Capacity[a]	Ratio[b]
7	37.11	37.54	31.83	32.21	34.25	34.65	17.88	18.09	36.91	0.00
14	82.23	44.80	79.00	43.04	80.59	43.91	54.97	29.95	82.22	37.34
28	166.49	47.22	163.47	46.36	164.24	46.58	121.00	34.31	166.32	44.80
42	249.64	48.04	246.64	47.46	246.60	47.45	189.74	36.51	249.14	47.17
84	495.61	49.06	491.93	48.70	489.57	48.46	411.18	40.70	493.85	47.94
140	818.19	49.55	813.16	49.24	807.83	48.92	730.30	44.23	815.58	48.89

[a]Capacity of the total sequestered carbonates, 10^3 kg

[b]Carbonatization efficiency of the injected aqueous CO_2, %

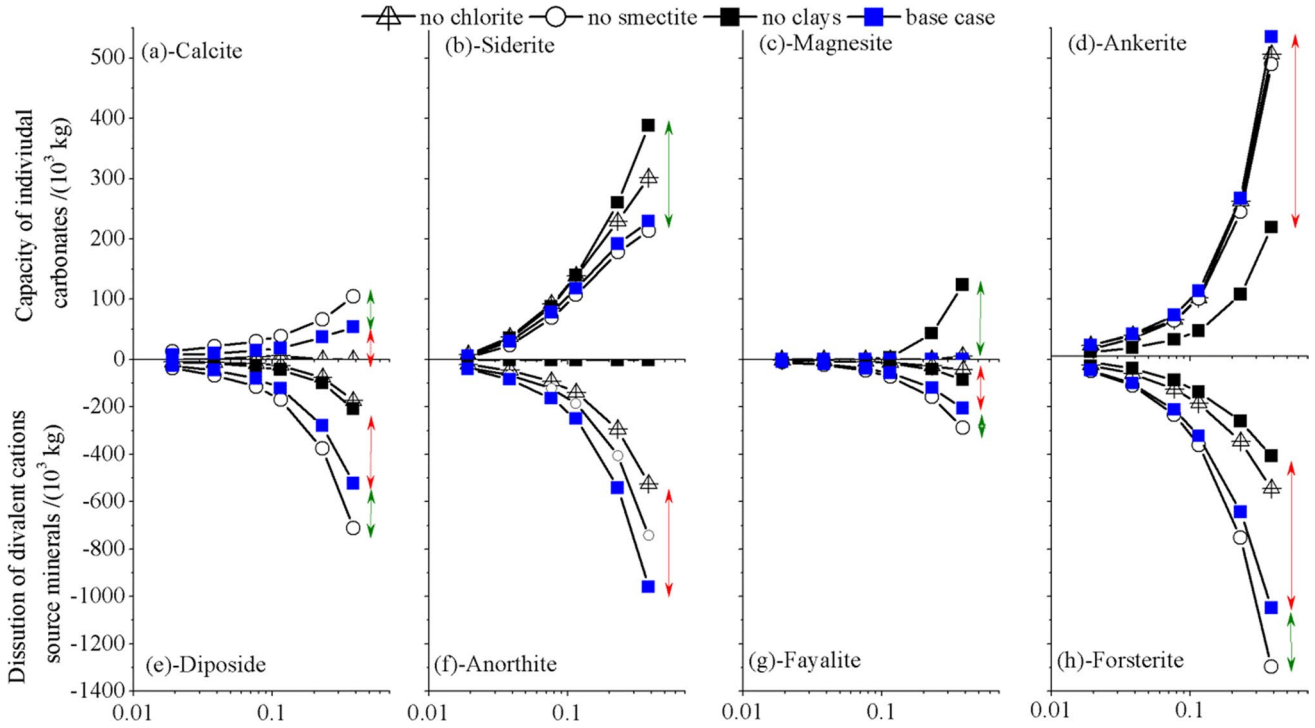

Fig. 5 Precipitation of the major carbonates (**a**, **b**, **c**, **d**, **e**) and dissolution of the divalent cations source minerals (**f**, **g**, **h**, **i**) for base_case, case_sm, case_chl and case_ncwp

of calcite was reduced due to the precipitation of smectite. Both chlorite and smectite compete with magnesite for Mg^{2+}. However, there is an exception for anorthite, the dissolution of which can release the needed divalent cations and alumino-silicate cations for smectite precipitation. Anorthite combined with diopside is also the major Ca^{2+} providers for the precipitation of ankerite and calcite. As seen in Fig. 5(f), the precipitation of chlorite and smectite both promoted the dissolution of anorthite, so as to promote the carbonatization of CO_2 into calcite and ankerite.

Figure 6 shows the spatial distribution of porosity, HCO_3^-, and pressure at 140 days for different simulation cases. The result of permeability distribution was not showed because it displayed with the same tendency with porosity. As seen, the competitive precipitation of clays can dramatically affect the evolution of reservoir porosity and permeability. The basalt showed a self-limiting trend in conductivity when clays were competitvely precipitated. However, a self-enhacing mode occurred when clays did not exist. It is reported that the smectite formation will clog narrow fractures and pore throats of the basalt, so as to decrease rock conductivity (Menefee et al. 2017), which is also the case in this study. Injectivity is closely related with the reservoir pressure perturbation (Heath et al. 2014; Liu et al. 2016, 2017). As shown in Fig. 6e and f, clay precipitation impacts the reservoir pressure evolution to a pronounced extent. To quantify the impact of clay precipitation on CO_2 injectivity, the peak pressure buildup of case_base and case_ncwp, which was 4.37 MPa and 2.76 MPa, was compared.

Cases with different injection rate

As shown in Fig. 7a, CO_2 mineralization efficiency increases with the decreasing of injection rate. Injection rate not only plays a vital role on the determining of the CO_2-water-basalt reaction extent but also exerts some effect on the reaction direction. As seen in Fig. 7b, the competing reactions between carbonates and clays for major divalent cations were affected by the extent of reaction with smectites and chlorite (Gysi and Stefánsson 2012a). The precipitation capacity of calcite and ankerite both decrease with the injection rate, but siderite displays a negative relationship with the injection rate. The reduction precipitation of chlorite with injection rate leads to the enhancement of siderite precipitation. Although smecite will also compete for Ca^{2+} with calcite, extended retention times (lower injection rate) mainly strengthen the precipitation of smectite and promote the disssolution of the two minerals (diopside and anorthite) serving as Ca source, thus to enhance calcite and ankerite precipitation. But higher injection rate limits the precipitation of smectite and reduce the formation of calcite and ankerite. Figure 7a also illustrated that the peak pressure of reservoir responded to CO_2 saturated water injection not monotonously increasing with injection rate. There is a

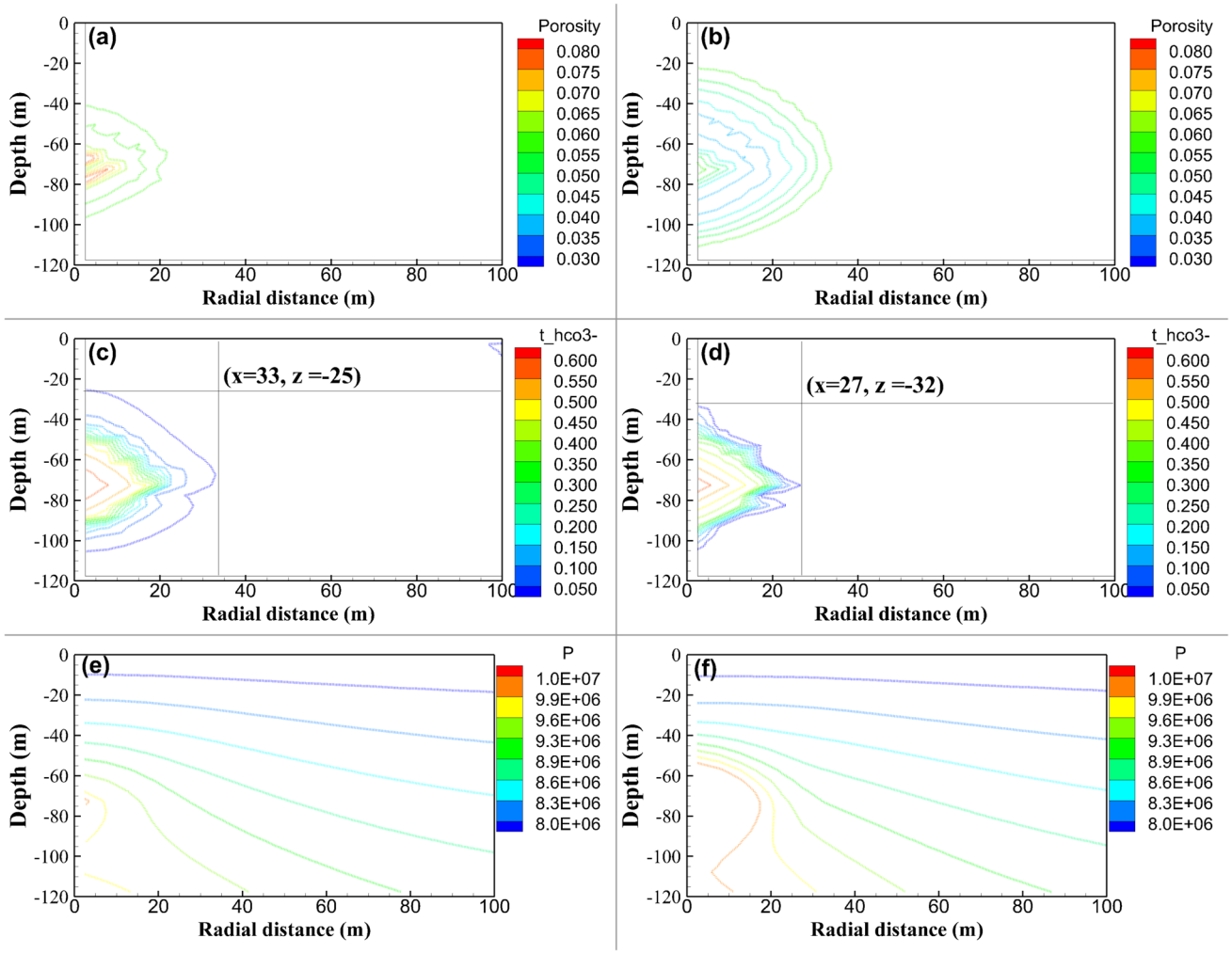

Fig. 6 Impact of clay precipitation on basalt porosity (**a**, **b**), CO2 migration (**c**, **d**), and reservoir pressure perturbation (**e**, **f**). a, c, e Case without consideration of clay precipitation; b, d, f case considering the precipitation of clays

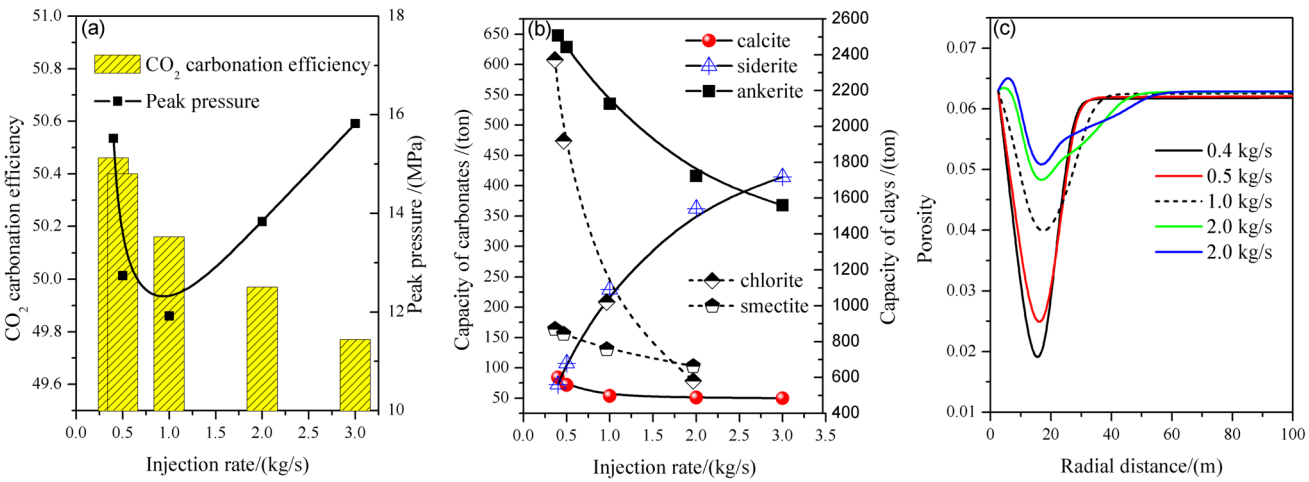

Fig. 7 CO2 carbonatization efficiency and reservoir peak pressure variation with injection rate (**a**); evolution of the capacity of major secondary minerals with injection rate (**b**); porosity distribution along the horizontal of the injection site at different injection rates (**c**)

critical injection rate, r_c, that existed. When $r < r_c$, pressure buildup decreases with the injection rate, but if $r > r_c$, pressure buildup increases with the injection rate.

Discussion

CO_2 sequestration potential of the Deccan basalt from the Mandla lobe

The CO_2 mineralization efficiency of the Deccan basalt in the Mandla lobe is about 50% at this specific condition within the duration of 140 days. It is similar to the first phase of the CarFix2 project which was reported that 50% of injected carbon and 76% of sulfur mineralized within 4 to 9 months (Clark et al 2020). The majority of the aqueous CO_2 is sequestered in ankerite, siderite, and calcite, which occupies a percent of 65%, 28%, and 7%, respectively. Apart from those carbonates, significant clays including chlorite and smectite also precipitated, among which chlorite is the major precipitated clays (57%) and smectite dominated the percentage of 43%. The results of Ca^{2+} resealing from the dissolution of olivine, pyroxene, and plagioclase being incorporated into calcite and ankerite, and Mg, Fe, and Si into smectite and chlorite, is similar to the study of Gysi and Stefánsson (2012b).

However, the results of the field-scale model are different from the lab-scale results, where calcite and aragonite were the dominated precipitated carbonates. Kanakiya et al. (2017) investigated the secondary mineralogy of basalt cores under CO_2(aq) imbibition and also observed ankerite to be the key secondary carbonate phase in their study, at CO_2 partial pressure of 4.5 MPa and temperature of 100 ℃. The CO_2 pressure of the field-scale model was set about 7.7 MPa according to the reservoir initial pressure, while only 5 bar and 10 bars of CO_2 pressure was set for the lab-scale experiment. It is conjectured that the discrepancy of precipitated carbonate type was mainly caused by the injected CO_2 concentration and ankerite was preferring to precipitate at higher CO_2 concentration.

Effect of clay precipitation on CO_2 carbonatization

Clays, zeolites, and oxides are widely observed to co-precipitate with carbonates in the context of CO_2-water-basalt reactions. Reaction path modeling have predicted precipitation of smectites and zeolites along with chalcedony, kaolinite, and goethite (Pham et al. 2012; Gysi and Stefánsson 2008). Several experimental studies also observed the formation of smectite at lower pH (Xiong et al. 2017; Hellevang et al. 2017). Some of the studies argued that the Mg^{2+} and Fe^{2+} cations released from the primary source minerals were incorporated into clay minerals such as smectites and oxides, and compete with the formation of magnesite and other carbonate minerals (Phukan et al 2020), whereas zeolites compete with calcite for dissolved Ca (Aradottir et al. 2012). Other studies also show that smectite or zeolite precipitation makes no contribution to the carbonatization of CO_2 (Menefee et al. 2017). In this study, we found that the precipitation of clays could enhance the mineralization of CO_2 in two pathways.

Firstly, the precipitation of smectite and chlorite will consume significant amount of divalent cations including Ca, Mg, Fe, and remarkable Si and Al in acid environment (Amram and Ganor, 2005; Bontognali et al. 2014; Peretyazhko et al. 2018). The formation water can be also acidified with chlorite precipitation so as to promote the dissolution of pyroxene, olivine, and plagioclase. Consequently, the precipitation of calcite was promoted by the generation of chlorite. It is reported that siderite was the most favorable carbonate precipitate under low pH conditions given comparable amount of available Ca^{2+}, Mg^{2+}, and Fe^{2+} (Adeoye et al. 2017). However, higher pH is more advantageous for the formation of siderite in this study (Fig. 5(c)). That is because at lower pH, chlorite will compete for Fe^{2+} with siderite, so as to limit the precipitation of siderite. Smectite precipitation will improve the dissolution of Ca-bearing minerals (diopside and anorthite) and to increase the precipitation capacity of calcite and ankerite.

Secondly, the clay precipitation will reduce reservoir conductivity to prolong the retention time for geochemical reactions. Clay precipitation not only exerts influence on the carbonatization of CO_2, but also impacts the porosity and permeability of basalt, potentially reduce CO_2 injectivity and affect the transportation of CO_2 (Hellevang et al. 2017). Menefee et al. (2017) and Liu et al. (2019) all indicated that increasing the retention time of aqueous CO_2 in the pore space can strengthen the mineralization of CO_2. Compared with the case_base, the total precipitated carbonates for case without consideration of porosity reduction response to conductivity (case_wcnp) were 815.58 tons, with a decline of 0.32% on CO_2 mineralization efficiency. However, 10.74% CO_2 carbonatization efficiency was reduced for case without consideration of the clay precipitation (case_ncwp).

Basalt conductivity evolution response to aqueous CO_2 injection

Except for clay precipitation, injection rate also impacts the mineralization of CO_2 in basaltic reservoir. A large numbers of studies reported the positive correlation between reservoir pressure buildup and fluid injection rate (Liu et al. 2017, 2016; Buscheck et al 2012, 2014). However, in basaltic reservoir, lower injection rate lead to

longer retention time of dissolved CO_2 in the pore space, so as to exaggerate the geochemical reaction between CO_2-water-basalt and enhance the pressure. Conventionally, the reservoir pressure buildup is determined with the injection rate for CO_2 sequestration in deep saline aquifer. However, in basaltic reservoir, the pressure buildup was not only caused by the expansion of reservoir pore space and compression of fluid in response to ex-situ fluid injection (occupies a weight of 63% for the baseline case), but also induced by the permeability and porosity reduction responding to clays precipitation and dominate a weight of 37% (Fig. 7c).

The pressure buildup is in positive relation with CO_2 injection rate and negative to rock conductivity (Liu et al. 2016), and the minimum pressure buildup will be obtained at the critical injection rate (as shown in Fig. 7a). To maximize CO_2 mineralization efficiency, it is reasonable to decrease the CO_2 injection rate; however, lower injection rate leads to the larger pressure buildup. In this study, the CO_2 mineralization efficiency variation deviation was only ~ 1.6% at the injection rate between 0.4 ~ 3.0 kg/s. Therefore, from the perspective of pressure supervision, to maintain the minimum pressure buildup while ensuring high CO_2 mineralization efficiency, 1.0 kg/s is much superior than 0.4 kg/s as well as 3.0 kg/s in this study.

Uncertainty analysis

Due to the lack of detailed data on the geological and hydrological conditions of the Deccan basalt from the Mandla lobe, this study is a robust preliminary assessment of the aqueous CO_2 geological sequestration potential. Although the benchmark model was established and reliable mineral reaction parameters were obtained by validating with the experimental data, the mineral composition of the basalt was only represented by one shale sample from the Mandla lobe. Uncertainty still existed on the selection of the basalt mineral compositions. It is reported that despite containing similar mineralogy, major oxides, and dissolution kinetics, different basalt types, e.g the Columbia River, Central Atlantic Mafic, Newark Basin, Deccan, and Karoo basalt, show different rates of CO_2 mineralization, composition, and morphologies of the neo-formed carbonates and silicates (Schaef et al 2010, 2009). CO_2 transport in basalt is also an important factor affecting CO_2 carbonatization, which is quite dependent on the rock porosity and permeability. Studies reported that pure advection flow with shorter retention times promotes rapid initial carbonatization, while pure diffusion sustains mineral reactions for longer time frames and generates greater net carbonatization net volumes (Liu et al. 2019; Menefee et al. 2017). In addition, the uncertainty on formation salinity and in situ reservoir temperature should also be considered. A series of studies have revealed that increased temperature and salinity enhanced the dissolution of the divalent-bearing minerals (Adeoye et al. 2017; Hellevang et al 2017). These uncertainties should be considered in the future studies.

Conclusions

In this study, reactive transport models are developed and verified based on the static batch lab-scale experiments and extended to the 2-D field-scale model to evaluate the CO_2 mineralization efficiency of the Deccan basalt from the Mandla lobe in India. Over 50% of the injected carbon can be mineralized into ankerite, siderite, and calcite within 140 days, and occupies a percent of 65%, 28%, and 7%, respectively. Apart from those carbonates, significant clays including chlorite and smectite also precipitated, among which chlorite is the major precipitated clays (57%) and smectite dominated the percentage of 43%. Precipitation of clays enhanced the mineralization of CO_2 in three pathways via (a) releasing H^+ to promote the dissolution of pyroxene, olivine, and plagioclase by chlorite precipitation; (b) consuming Si and Al to improve the dissolution of Ca source minerals including diopside and anorthite and increase the precipitation of calcite and ankerite; and (c) reducing reservoir conductivity to prolong the retention time for geochemical reactions. But the competition for Ca^{2+}, Mg^{2+}, and Fe^{2+} between smectite, chlorite, and calcite, and siderite also occurred. In basaltic reservoir, CO_2 mineralization efficiency as well as the pressure build-up increases with the reduction of injection rate. However, extreme pressure perturbation will limit the injectivity and enhance the storage security; thus, the CO_2 injection rate should be precisely designed to maximize the CO_2 carbonatization efficiency and ensure safety. Due to the lack of detailed data on the geological and hydrological conditions of the Deccan basalt from the Mandla lobe, uncertainty on the basalt mineral composition, reservoir porosity and permeability, reservoir initial temperature and pressure, etc. still existed. To obtain a more accuracy evaluation results, detailed and complicated 3-D model should be established in the future.

Nomenclature r_n: The kinetic reaction rate; k_n: The rate constant which is temperature and pH dependent; k_{25}: The reaction rate constant at 25ºC; A_n: The specific reactive surface area per kg H_2O of each mineral, cm^2/g; Ω_n: The kinetic mineral saturation ratio; E_a.: The activation energy; R: Gas constants; T: Absolute temperature, K; nu, H, and OH: Indicate neutral, acid, and base mechanisms; a: The activity of the species; σ: Power term; i: Index of the ith grid in the field-scale model; $\varnothing_0$: The initial porosity of the ith grid; k_0: The initial permeability of the ith grid; $\varnothing_i$: The current porosity of the ith grid; k_i: The current permeability of the ith grid; k: Number of the kth carbonates; l: The total precipitated carbonates; t: The injection time, s; V_i: The

volume of ith grid, m^3; F_k^i: The volume fraction of kth mineral in ith grid, %; F_n^i: The volume fraction of the inactive grid, %; ρ_k: The density of the kth carbonates, kg/m^3; M_k: The molar weight of the kth carbonates, g; b: The stoichiometric number of carbon in kth carbonates; $c_{co2(aq)}^{inj}$, c_{hco3-}^{inj}: The molar concentration of CO_2(aq) and HCO_3^- in the injected water, mole/kgH_2O; $c_{co2(aq)}^{ini}$, c_{hco3-}^{ini}: The molar concentration of CO_2(aq) and HCO_3^- in the initial water, mole/kgH_2O; r: The injection rate, kg/s; m_k^t: The total mass of carbon in precipitated carbonates k at time t, kg; ${m_{DIC}}^t$: The total DIC at time t, kg; E: The carbon mineralization efficiency,

Supplementary Information The online version contains supplementary material available at https://doi.org/10.1007/s11356-022-21757-y.

Acknowledgements We appreciate the help of Professor Shrivastava and his research group in the Department of Geology of Delhi University in India for providing important data for validation of our lab-scale numerical model.

Author contribution Danqing Liu: conceptualization; methodology; validation; formal analysis; writing—original draft; funding acquisition
Ramesh Agarwal: conceptualization; resources; writing—review and editing; supervision
Fang Liu: investigation, data curation
Sen Yang: data curation
Yilian Li: writing—review and editing

Funding This work was funded by the National Natural Science Foundation of China (Grant No. 41902253) and the Fundamental Research Funds for the Central Universities, China University of Geosciences (Wuhan) (No. CUG192716).

Data availability Not applicable.

Declarations

Ethics approval and consent to participate Not applicable.

Consent for publication Not applicable.

Competing interests The authors declare no competing interests.

References

Abraham-A RM, Tassinari CCG (2021) CO_2 storage algorithms involving the hybrid geological reservoir of the Irati Formation, Parana Basin. Int J Greenhouse Gas Control 112:103504

Adeoye JT, Menefee AH, Xiong W, Wells RK, Skemer P, Giammar DE et al (2017) Effect of transport limitations and fluid properties on reaction products in fractures of unaltered and serpentinized basalt exposed to high PCO_2 fluids. Int J Greenhouse Gas Control 63:310–320

Amram K, Ganor J (2005) The combined effect of pH and temperature on smectite dissolution rate under acidic conditions. Geochim Cosmochim Acta 69(10):2535–2546

Andreani M, Luquot L, Gouze P, Godard M, Hoise E, Gibert B (2009) Experimental study of carbon sequestration reactions controlled by the percolation of CO_2-rich brine through peridotites. Environ Sci Technol 43(4):1226–1231

Aradottir ESP, Sonnenthal EL, Bjornsson J, Jonsson H (2012) Multidimensional reactive transport modeling of CO_2 mineral sequestration in basalts at the Hellisheidi geothermal field, Iceland. Int J Greenhouse Gas Control 9:24–40

Berner RA, Raiswell R (1983) Burial of organic carbon and pyrite sulfur in sediments over Phanerozoic time: a new theory. Geochim Cosmochim Acta 47(5):855–862

Bontognali TRR, Martinez-Ruiz F, McKenzie JA, Bahniuk A, Anjos S, Vasconcelos C (2014) Smectite synthesis at low temperature and neutral pH in the presence of succinic acid. Appl Clay Sci 101:553–557

Buscheck TA, Sun Y, Chen M, Hao Y, Wolery TJ, Bourcier WL et al (2012) Active CO_2 reservoir management for carbon storage: analysis of operational strategies to relieve pressure buildup and improve injectivity. Int J Greenhouse Gas Control 6:230–245

Buscheck TA, White JA, Chen M, Sun Y, Hao Y, Aines RD et al (2014) Pre-injection brine production for managing pressure in compartmentalized CO_2 storage reservoirs. Energy Procedia 63:5333–5340

Cadogan SP, Maitland GC, Trusler JPM (2014) Diffusion coefficients of CO2 and N2 in water at temperatures between 298.15 K and 423.15 K at pressures up to 45 MPa. J Chem Eng Data 59(2):519–525

Callow B, Falcon-Suarez I, Ahmed S et al (2018) Assessing the carbon sequestration potential of basalt using X-ray micro-CT and rock mechanics. Int J Greenhouse Gas Control 70:146–156

IPCC (2005) Special report on carbon dioxide capture and storage, IPCC, Cambridge, the UK and New York, USA

Clark DE, Oelkers EH, Gunnarsson I, Sigfússon B, Snæbjörnsdóttir SÓ, Aradóttir ES et al (2020) CarbFix2: CO2 and H2S mineralization during 3.5 years of continuous injection into basaltic rocks at more than 250 °C. Geochimica et Cosmochimica Acta 279:45–66

Gislason OSR (2001) The mechanism, rates and consequences of basaltic glass dissolution: I. An experimental study of the dissolution rates of basaltic glass as a function of aqueous Al, Si and oxalic acid concentration at 25°C and pH = 3 and 11. Geochimica et Cosmochimica Acta 65(21):3671–3681

Gislason SR, Wolff-Boenisch D, Stefansson A, Oelkers EH, Gunnlaugsson E, Sigurdardottir H et al (2010) Mineral sequestration of carbon dioxide in basalt: a pre-injection overview of the CarbFix project. Int J Greenhouse Gas Control 4(3):537–545

Gysi AP, Stefánsson A (2008) Numerical modelling of CO_2-water-basalt interaction. Mineral Mag 72(1):55–59

Gysi AP, Stefánsson A (2012a) Mineralogical aspects of CO_2 sequestration during hydrothermal basalt alteration — an experimental study at 75 to 250°C and elevated pCO_2. Chem Geol 306–307:146–159

Gysi AP, Stefánsson A (2012b) Experiments and geochemical modeling of CO_2 sequestration during hydrothermal basalt alteration. Chem Geol 306–307:10–28

Heath JE, McKenna SA, Dewers TA, Roach JD, Kohos PH (2014) Multiwell CO_2 injectivity: impact of boundary conditions and brine extraction on geologic CO_2 storage efficiency and pressure buildup. Environ Sci Technol 48(2):1067–1074

Hellevang H, Haile BG, Tetteh A (2017) Experimental study to better understand factors affecting the CO2 mineral trapping potential of basalt. Greenhouse Gas Sci Technol 7(1):143–157

Kanakiya S, Adam L, Esteban L, Rowe MC, Shane P (2017) Dissolution and secondary mineral precipitation in basalts due to reactions with carbonic acid. J Geophys Res Solid Earth 122(6):4312–4327

Keller G, Adatte T, Gardin S, Bartolini A, Bajpai S (2008) Main Deccan volcanism phase ends near the K-T boundary: evidence from the Krishna-Godavari Basin, SE India. Earth Planet Sci Lett 268(3–4):293–311

Krishnamurthy P (2020) The Deccan Volcanic Province (DVP), India: a review. J Geol Soc India 96(1):9–35

Kumar A, Shrivastava JP (2019a) Long-term CO_2 capture-induced calcite crystallographic changes in Deccan basalt, India. Environ Earth Sci 78(13):376. https://doi.org/10.1007/s12665-019-8378-x

Kumar A, Shrivastava JP (2019b) Thermodynamic modelling and experimental validation of CO_2 mineral sequestration in Mandla Basalt of the Eastern Deccan Volcanic Province, India. J Geol Soc India 93(3):269–277

Kumar A, Shrivastava JP (2019c) Carbon capture induced changes in Deccan basalt: a mass-balance approach. Greenhouse Gas Sci Technol 9(6):1158–1180

Kumar A, Shrivastava JP, Pathak V (2017) Mineral carbonatization reactions under water-saturated, hydrothermal-like conditions and numerical simulations of CO_2 sequestration in tholeiitic basalt of the Eastern Deccan Volcanic Province, India. Applied Geochemistry: S0883292717302196

Lasaga AC, Soler JM, Ganor J, Burch TE, Nagy KL (1994) Chemical weathering rate laws and global geochemical cycles ☆. Geochim Cosmochim Acta 58(10):2361–2386

Li X, Kind R, Yuan X, Woelbern I, Hanka W (2004) Rejuvenation of the lithosphere by the Hawaiian plume. Nature 427(6977):827–829

Liu D, Agarwal R, Li Y (2016) Numerical simulation and optimization of CO_2 -enhanced water recovery by employing a genetic algorithm. J Clean Prod 133:994–1007

Liu D, Agarwal R, Li Y (2017) Numerical simulation and optimization of CO_2 enhanced shale gas recovery using a genetic algorithm. J Clean Prod 164:1093–1104

Liu D, Agarwal R, Li Y, Yang S (2019) Reactive transport modeling of mineral carbonatization in unaltered and altered basalts during CO_2 sequestration. Int J Greenhouse Gas Control 85:109–120

Manning CE, Bird DK (1995) Porosity, permeability, and basalt metamorphism. Geological Society of America 296:123–140

Marieni C, Henstock TJ, Teagle DAH (2013) Geological storage of CO_2 within the oceanic crust by gravitational trapping. Geophys Res Lett 40(23):6219–6224

Matter JM, Stute M, Snæbjörnsdottir SÓ, Oelkers EH, Gislason SR, Aradottir ES et al (2016) Rapid carbon mineralization for permanent disposal of anthropogenic carbon dioxide emissions. Science 352(6291):1312–1314

McGrail BP, Schaef HT, Ho AM, Chien YJ, Dooley JJ, Davidson CL (2006) Potential for carbon dioxide sequestration in flood basalts. J Geophys Res 111(B12)

Menefee AH, Li P, Giammar DE, Ellis BR (2017) Roles of transport limitations and mineral heterogeneity in carbonatization of fractured basalts. Environ Sci Technol 51(16):9352–9362

Nicolas S, Pruess K et al (2003) CO2-H2O mixtures in the geological sequestration of CO_2. I. Assessment and calculation of mutual solubilities from 12 to 100°C and up to 600 bar. Geochimica Et Cosmochimica Acta 67(16):3015–3031

Palandri JL, Kharaka YK (2004) A compilation of rate parameters of water-mineral interaction kinetics for application to geochemical modeling. Geological Survey Menlo Park CA

Pattanayak JPSK (2002) Basalts of the Eastern Deccan Volcanic Province, India. Gondwana Res 5(3):649–665

Pawar NJ, Pawar JB, Kumar S, Supekar A (2008) Geochemical eccentricity of ground water allied to weathering of basalts from the Deccan Volcanic Province, India: insinuation on CO_2 consumption. Aquat Geochem 14(1):41–71

Peretyazhko TS, Niles PB, Sutter B, Morris RV, Agresti DG, Le L et al (2018) Smectite formation in the presence of sulfuric acid: implications for acidic smectite formation on early Mars. Geochim Cosmochim Acta 220:248–260

Perumal SK (2014) Petrophysical properties of the Deccan basalts exposed in the Western Ghats escarpment around Mahabaleshwar and Koyna, India. J Asia Earth Sci 84(8):176–187

Peuble S, Godard M, Luquot L, Andreani M, Martinez I, Gouze P (2015) CO_2 geological storage in olivine rich basaltic aquifers: new insights from reactive-percolation experiments. Appl Geochem 52:174–190

Pham T, Aagaard P, Hellevang H (2012) On the potential for CO_2 mineral storage in continental flood basalts – PHREEQC batch- and 1D diffusion–reaction simulations. Geochemical Transactions 13. https://doi.org/10.1186/1467-4866-13-5

Phukan M, Hong PV, Haese RR (2020) Mineral dissolution and precipitation reactions and their net balance controlled by mineral surface area: an experimental study on the interactions between continental flood basalts and CO2-saturated water at 80 bars and 60°C. Chem Geol 559:119909

Pokrovsky OS, Golubev SV, Schott J (2005) Dissolution kinetics of calcite, dolomite and magnesite at 25 C and 0 to 50 atm pCO_2. Chem Geol 217(3–4):239–255

Prasad PSR, Sarma DS, Sudhakar L, Basavaraju U, Charan SN (2009) Geological sequestration of carbon dioxide in Deccan basalts: preliminary laboratory study. Currentence 96(2):288–291

Pruess K (1991) TOUGH2: a general-purpose numerical simulator for multiphase fluid and heat flow. Nasa Sti/recon Technical Report N 92

Pruess K, Oldenburg CM, Moridis GJ (1999) TOUGH2 User's Guide Version 2. Office of Scientific & Technical Information Technical Reports

Ragnheidardottir E, Sigurdardottir H, Kristjansdottir H, Harvey W (2011) Opportunities and challenges for CarbFix: an evaluation of capacities and costs for the pilot scale mineralization sequestration project at Hellisheidi, Iceland and beyond. Int J Greenhouse Gas Control 5(4):1065–1072

Rani N, Pathak V, Shrivastava JP (2013) CO_2 mineral trapping: an experimental study on the carbonatization of basalts from the Eastern Deccan Volcanic Province, India. Procedia Earth & Planetary Science 7:806–809

Schaef HT, McGrail BP, Owen AT (2009) Basalt-CO_2-H_2O interactions and variability in carbonate mineralization rates. In: Gale J, Herzog H and Braitsch J (J. Gale, H. Herzog and J. Braitsch (Eds.), 9th International Conference on Greenhouse Gas Control Technologies, pp. 4899–4906

Schaef HT, McGrail BP, Owen AT (2010) Carbonate mineralization of volcanic province basalts. Int J Greenhouse Gas Control 4(2):249–261

Shrivastava J, Pathak V (2016) Geochemical Modeling and Experimental Studies on Mineral Carbonatization of Primary Silicates for Long-term Immobilization of CO_2 in Basalt from the Eastern Deccan Volcanic Province. Journal of Indian Geophysical Union, Special Volume: pp: 42–58

Shrivastava JP, Mahoney JJ, Kashyap MR (2014) Trace elemental and Nd-Sr-Pb isotopic compositional variation in 37 lava flows of the Mandla lobe and their chemical relation to the western Deccan stratigraphic succession, India. Miner Petrol 108(6):801–817

Snæbjörnsdóttir SÓ, Gislason SR, Galeczka IM, Oelkers EH (2018) Reaction path modelling of in-situ mineralisation of CO_2 at the CarbFix site at Hellisheidi, SW-Iceland. Geochimica Et Cosmochimica Acta 220:348–366

Srinivas KNSS, Kishore PP, Rao DVS (2019) The geological site characterisation of the Mandla region, Eastern Deccan Volcanic Province, Central India. J Earth Syst Sci 128(5):139

Steefel CI (1994) A coupled model for transport of multiple chemical species and kinetic precipitation/dissolution reactions phase application to reactive flow in single phase hydrothermal systems. Amer J Sci 294(5):529–592

Talman S (2015) Subsurface geochemical fate and effects of impurities contained in a CO_2 stream injected into a deep saline aquifer: what is known. Int J Greenhouse Gas Control 40:267–291

Unit TECI (2020) Net zero: why is it necessary? https://www.theiet.org/impact-society/sectors/education-and-skills/education-and-skills-blog-posts/what-is-net-zero-and-why-is-it-necessary/. Accessed 07-04-2022

USGS (2020) Groundwater age. https://www.usgs.gov/mission-areas/water-resources/science/groundwater-age?. Accessed 07-04-2022

Wolff-Boenisch D, Galeczka IM (2018) Flow-through reactor experiments on basalt-(sea)water-CO_2 reactions at 90°C and neutral pH. What happens to the basalt pore space under post-injection conditions? Int J Greenhouse Gas Control 68:176–190

Xiong W, Wells RK, Menefee AH, Skemer P, Ellis BR, Giammar DE (2017) CO2 mineral trapping in fractured basalt. Int J Greenhouse Gas Control 66:204–217

Xu T, Sonnenthal E, Spycher N, Pruess K (2006) TOUGHREACT—a simulation program for non-isothermal multiphase reactive geochemical transport in variably saturated geologic media: applications to geothermal injectivity and CO_2 geological sequestration. Comput Geosci 32(2):145–165

Yeh GT, Tripathi VS (1991) A model for simulating transport of reactive multispecies components: model development and demonstration. Water Resour Res 27(12):3075–3094

Zhu C, Liu Z, Zhang Y, Wang C, Scheafer A, Lu P, Zhang G, Georg RB, Yuan H, Rimstidt JD (2016) Measuring silicate mineral dissolution rates using Si isotope doping. Chem Geol 445:146–163